Modeling convection heat transfer and turbulence with fire applications: a high temperature vertical plate and a methane fire

By D. Rouson †, S. R. Tieszen ‡ AND G. Evans ¶

Simulations of the three-dimensional turbulent flow and heat transfer adjacent to a large (3 meter) high temperature (up to 860 K) vertical flat plate and in a large-scale methane flame have been made and compared with experimental data. Results are obtained with a Reynolds averaged Navier-Stokes (RANS) $v^2 - f$ model, a direct numerical simulation (DNS), and a detached eddy simulation (DES) model. The preliminary results are encouraging, with respect both to heat transfer and to the prediction of large-scale structures in these highly buoyant flow fields.

1. Motivation and objectives

Although radiation is the dominant heat-transfer mechanism in fires, turbulent convection to or from a surface can be significant. The convective regime typically encountered in fires is turbulent mixed convection. Due to large surfaces and large temperature differences, the Grashof number in fires can be quite high, e.g. 1.0×10^{12}, and the effects of variable properties can be significant. Turbulent mixed-convection heat transfer from a large (3 meter) vertical, high-temperature (T_{surface} up to 860K) surface was studied experimentally by Siebers, Schwind & Moffat (1983). In that study, local and average heat transfer coefficients as well as boundary layer profiles of velocity and temperature were obtained; these quantities can be used for validation of computer models of turbulent convection heat transfer dint conditions commonly encountered in fires. The present work describes three approaches that use different formulations to solve the Navier-Stokes and energy equations to predict the flow and heat transfer from a large, high temperature vertical surface. These three methods are: 1) a RANS formulation using the $v^2 - f$ model in an unstructured-control-volume finite-element code to predict the steady flow and heat transfer; 2) a DNS formulation of the unsteady free convection turbulent boundary layer on the high-temperature plate; and 3) a DES formulation that uses time filtering to allow large-scale time-dependent structures to be captured. Preliminary results were obtained during the summer program and are described in the following sections of this report.

2. RANS $v^2 - f$ modeling of mixed and forced convection

2.1. *Problem description and cases selected for simulation*

The problem studied is shown in figure 1. Air flows horizontally at constant freestream velocity parallel to the surface (xy plane) of a 3 m by 3 m vertical flat plate. In the experiment the plate surface consisted of 21 stainless steel strips oriented horizontally

† City College of the City University of New York, NY
‡ Sandia National Laboratories, Albuquerque, NM
¶ Sandia National Laboratories, Livermore, CA

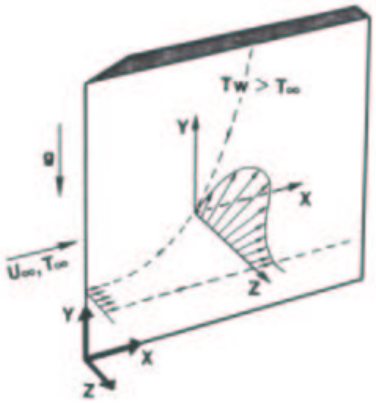

FIGURE 1. Flat plate geometry.

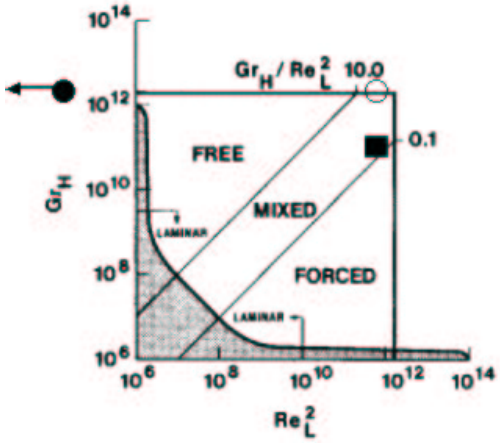

FIGURE 2. Flow regime map showing the three cases selected for simulation; filled circle: free convection ($\mathrm{Gr_H} = 1.4 \times 10^{12}$, $\mathrm{Re_L} = 0.0$, $\mathrm{Gr_H/Re_L}^2 = \infty$); open circle: mixed convection ($\mathrm{Gr_H} = 2.3 \times 10^{12}$, $\mathrm{Re_L} = 8.7 \times 10^5$, $\mathrm{Gr_H/Re_L}^2 = 3.06$); filled square: forced convection dominated ($\mathrm{Gr_H} = 1.4 \times 10^{11}$, $\mathrm{Re_L} = 8.9 \times 10^5$, $\mathrm{Gr_H/Re_L}^2 = 0.18$).

(from x=0 to L) with an electrical current passing through each strip to give uniform heat flux through the surface. The plate surface temperature was measured at 105 locations with thermocouples. These measured surface temperatures were used in the current study as the thermal boundary condition at the surface of the plate ($z = 0$). Figure 2 shows the flow regime studied experimentally in terms of dimensionless parameters, $\mathrm{Gr_H}$ and $\mathrm{Re_L}$, where

$$\mathrm{Gr_H} = \frac{g\beta(T_w - T_\infty)\mathrm{H}^3}{\nu^2} \qquad \mathrm{Re_L} = \frac{u_\infty \mathrm{L}}{\nu}, \tag{2.1}$$

and the cases selected for the numerical study.. The properties of air that enter these dimensionless parameters were evaluated at ambient temperature (T_∞) and pressure; H and L are the vertical and horizontal plate dimensions, respectively. The three cases selected for simulation span the range of the experiment: they are; (1) a forced-convection-

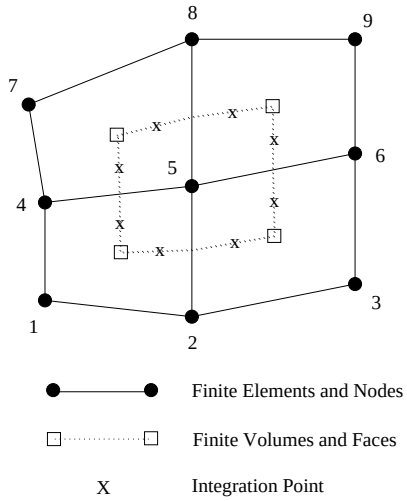

FIGURE 3. A control volume centered about a finite-element node in a collection of 2D quadrilateral elements.

dominated flow condition (ID604) with $u_\infty = 4.4$ m/s, $\mathrm{Re_L} = 8.9{\times}10^5$, $T_w \approx 323$ K, $\mathrm{Gr_H} = 1.4 \times 10^{11}$, $\mathrm{Gr_H/Re_L}^2 = 0.18$; (2) a free-convection flow condition (ID643) with $T_w \approx 698$ K, $\mathrm{Gr_H} = 1.4 \times 10^{12}$; and (3) a mixed-convection flow condition (ID648) with $u_\infty = 4.3$ m/s, $\mathrm{Re_L} = 8.7 \times 10^5$, $T_w \approx 829$ K, $\mathrm{Gr_H} = 2.3 \times 10^{12}$, $\mathrm{Gr_H/Re_L}^2 = 3.06$.

The high temperatures of the mixed- and free-convection cases result in significant property variations across the boundary layer and a radiation heat transfer that is 38% to 50% of the electrical energy dissipated in the surface. The heat transfer by radiation and by conduction through the back surface of the plate was accounted for in determining the local heat transfer coefficient, which had an experimental uncertainty ranging from 6% to 10%.

2.2. *Numerical method*

The numerical model is a low-Mach-number, variable-property formulation of the Reynolds-averaged Navier-Stokes (RANS), energy, species, and mass-conservation equations. Developed at Sandia National Laboratories as part of the Department of Energy's Accelerated Strategic Computing Initiative (ASCI) project, Fuego is a control volume finite element code for the simulation of the fluid mechanics and heat transfer in fires (Moen, Evans, Domino & Burns (2002)). Combustion is modeled with the Eddy Dissipation Concept (EDC) of Magnussen (1989); the default turbulence model is the standard $k-\epsilon$ model of Launder & Spalding (1974). Recently the $v^2 - f$ model of Durbin (1991) has been added as an option, and is used in this study. Transport equations are included for 6 species and for the nucleation, growth, and transport of soot. For fire simulations Fuego is coupled with a discrete-ordinates finite-element participating-media radiation code, Syrinx (Burns (1997)). Fuego and Syrinx are two modules of a larger suite of codes in the SIERRA framework (Edwards & Stewart (2001)) at Sandia. This framework provides a common architecture, allowing codes to be coupled to solve multi-mechanics problems. The framework provides access to linear solver packages, parallel tools, parsing tools, etc.

Variables in Fuego are collocated at the nodes of the mesh as shown in the control volume of figure 3 (shown as a 2D quadrilateral for convenience). A pressure-projection method is used together with pressure smoothing to satisfy continuity at each time step;

the equations are solved one at a time (segregated-solution method). Three-dimensional hex elements are supported currently with tetrahedral elements planned. The code is first-order accurate in time; various upwind convection discretizations yield overall spatial accuracy between first and second order. The results presented here used first-order upwind differences. Fuego runs on a variety of computing platforms including Janus, the massively-parallel computer at Sandia.

The control-volume formulation of the turbulence model is:

$$\int \frac{\partial \rho k}{\partial t} dV + \int \rho k u_j n_j dS = \int \left(\mu + \frac{\mu_t}{\sigma_k}\right) \frac{\partial k}{\partial x_j} n_j dS + \int (P - \rho\epsilon) dV \tag{2.2}$$

$$\int \frac{\partial \rho \epsilon}{\partial t} dV + \int \rho \epsilon u_j n_j dS = \int \left(\mu + \frac{\mu_t}{\sigma_\epsilon}\right) \frac{\partial \epsilon}{\partial x_j} n_j dS + \int \frac{1}{T}(C'_{\epsilon_1} P - C_{\epsilon_2} \rho\epsilon) dV \tag{2.3}$$

$$\int \frac{\partial \rho \bar{v^2}}{\partial t} dV + \int \rho \bar{v^2} u_j n_j dS = \int (\mu + \mu_t) \frac{\partial \bar{v^2}}{\partial x_j} n_j dS + \int (\rho k f - \rho N \bar{v^2} \frac{\epsilon}{k}) dV \tag{2.4}$$

$$\int \frac{f}{L^2} dV - \int \frac{\partial f}{\partial x_j} n_j dS = \int \frac{1}{L^2} \left\{ C_1 \frac{(2/3 - \bar{v^2}/k)}{T} + C_2 \frac{P}{\rho k} + \frac{(N-1)\bar{v^2}/k}{T} \right\} dV \tag{2.5}$$

$$P = 2\mu_t S^2 - \frac{2}{3}\delta_{ij} \frac{\partial u_i}{\partial x_j} \left(\rho k + \mu_t \frac{\partial u_l}{\partial x_l}\right) \tag{2.6}$$

$$S^2 = S_{ij} S_{ij} = \frac{1}{4} \left(\frac{\partial u_i}{\partial x_j} + \frac{\partial u_j}{\partial x_i}\right) \left(\frac{\partial u_i}{\partial x_j} + \frac{\partial u_j}{\partial x_i}\right) \tag{2.7}$$

$$T = \max \left[\frac{k}{\epsilon} \, , 6\sqrt{\frac{\nu}{\epsilon}} \right] \tag{2.8}$$

$$L = C_L \max \left[\frac{k^{3/2}}{\epsilon} \, , C_\eta \left(\frac{\nu^3}{\epsilon}\right)^{1/4} \right] \tag{2.9}$$

$$\mu_t = C_\mu \rho \bar{v^2} T \tag{2.10}$$

$$C'_{\epsilon_1} = C_{\epsilon_1} \left(1 + 0.045\sqrt{k/\bar{v^2}}\right) \; ; \quad C_{\epsilon_1} = 1.4, \; C_{\epsilon_2} = 1.9, \; C_\mu = 0.22 \tag{2.11}$$

$$C_1 = 0.4, \; C_2 = 0.3, \; N = 6, \; C_L = 0.23, \; C_\eta = 70, \; \sigma_\epsilon = 1.0 \tag{2.12}$$

In the above equations, $k, u_j, \rho, n_j, \mu, P, \epsilon, \bar{v^2}, f, \nu,$ and μ_t are the turbulent kinetic energy, time averaged velocity, density, unit normal, dynamic viscosity, turbulent energy production rate, turbulent energy dissipation rate, wall-normal component of turbulent kinetic energy, elliptic relaxation variable, kinematic viscosity, and turbulent viscosity, respectively. The turbulent Prandtl number is assumed to be 0.9. At the surface of the plate ($z = 0$) the boundary conditions for the turbulence variables are

$$k = \bar{v^2} = f = 0; \quad \epsilon = 2\nu k_p {y_p}^2 \tag{2.13}$$

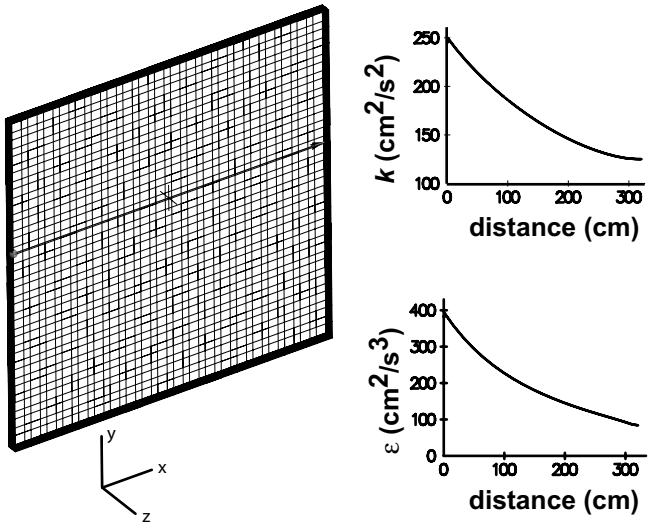

FIGURE 4. Curves of k and ϵ showing decay in the streamwise direction of the freestream values and mesh showing line along which curve data was taken (y=2 m; z=10 cm).

where variables with subscript p are assumed to be located at the centers of the surface node subcontrol volumes. For the forced and mixed convection cases, at the inflow boundary ($x = 0$), velocity, temperature, k, ϵ, and $\bar{v^2}$ are specified and $\partial f/\partial n = 0$. On the open boundaries: at y=0, H and at x=L and as $z \to \infty$, pressure is specified ($p = 0$), $\partial f/\partial n = 0$, and k, ϵ, and $\bar{v^2}$ are convected out of the domain with the calculated mass flow rate. If the flow is into the domain on the open boundaries, then k, ϵ, and $\bar{v^2}$ enter the domain with specified values.

2.3. *Forced convection dominated flow and heat transfer results*

In the forced convection dominated case selected for simulation, ID604, $\mathrm{Re_L} = 8.9\mathrm{x}10^5$ (the momentum thickness Reynolds number was approximately 1450 at x=2.75 m). In the experiment the boundary layer was tripped with a vertical wire located at x=0.65 m; effectively the upstream 30% of the boundary layer was laminar or transitional. To insure a turbulent boundary layer flow over the plate, the simulation used an inlet turbulent intensity of 3% and a length scale of 10 cm, resulting in inlet values of k and ϵ of 250 $\mathrm{cm^2/s^2}$ and 394 $\mathrm{cm^2/s^3}$, respectively; $\bar{v^2}$ was set to 70 $\mathrm{cm^2/s^2}$ at the inlet. The effects of buoyancy are small in this case ($\mathrm{Gr_H/Re_L}^2 = 0.18$). The 3D mesh used for the results shown in this report and curves showing the freestream (z=10 cm) decay of k and ϵ in the streamwise (x) direction at the height y=2 m are shown in figure 4. The mesh is $20 \times 20 \times 30$ in the (x, y, z) directions, uniform in x and y, and nonuniform in z such that $y^+ \approx 2$ at the first subcontrol volume off the surface.

Computed and measured boundary-layer profiles of temperature and the x component of velocity at x=276 cm, y=108 cm are compared in figures 5 and 6, respectively. The calculated results agree reasonably well with the data. The computed local heat-transfer coefficient is compared with experimental data in figure 7. Also shown in figure 7 is a 2D simulation result (symmetry boundary conditions were applied to the domain at y=0,

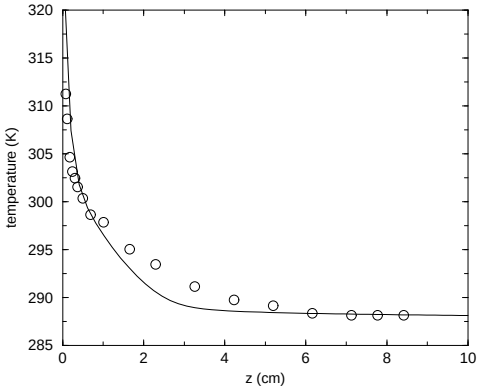

FIGURE 5. Comparison of calculated (line) and measured (symbols) boundary layer temperature profiles at x=276 cm, y=108 cm; forced convection dominated, ID604.

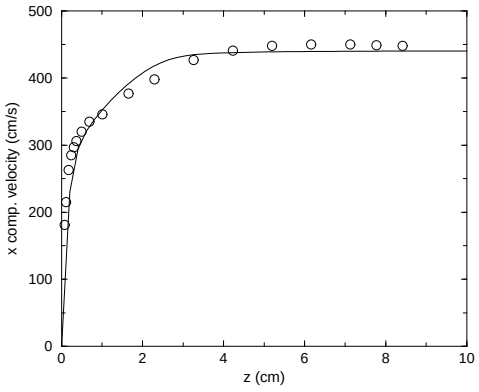

FIGURE 6. Comparison of calculated (line) and measured (symbols) boundary layer velocity profiles at x=276 cm, y=108 cm; forced convection dominated, ID604.

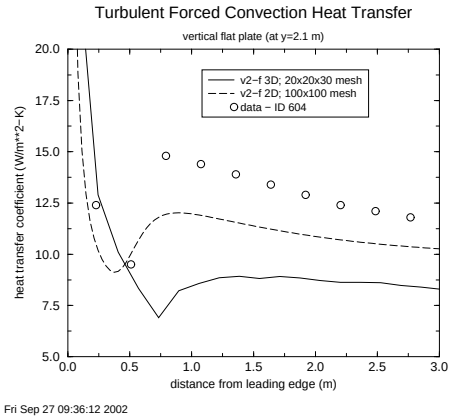

FIGURE 7. Local heat-transfer coefficient at y=2.1 m for the forced convection dominated case.

H) on a 100×100 mesh in the x, z plane with one element in the vertical (y) direction. Transition is evident where the heat transfer coefficient increases from a minimum value at $x \approx$60 cm. Note that the specified surface-temperature distribution implicitly includes the effects of transition; prediction of transition is not addressed here. The calculations agree qualitatively with the data. Medium- and fine-mesh 3D calculations are being made to reduce the uncertainty in the results due to mesh spacing.

2.4. *Mixed convection flow and heat transfer results*

The Reynolds number for the mixed-convection case selected for simulation, ID648, is $\mathrm{Re_L} = 8.7 \times 10^5$, similar to the forced convection dominated case. There was no trip wire in this experimental case; however there is evidence of transition at approximately the same horizontal location on the flat plate ($x \approx$0.65 m). As in the forced-convection-dominated case, the simulation used an inlet turbulent intensity of 3% and a length scale of 10 cm. The same $20 \times 20 \times 30$ 3D mesh was used for this case.

The effects of buoyancy are now significant ($\mathrm{Gr_H}/{\mathrm{Re_L}}^2 = 3.06$): the horizontal flow in the freestream over the plate undergoes significant turning toward the vertical (y) direction within the boundary layer. Computed and measured boundary-layer profiles

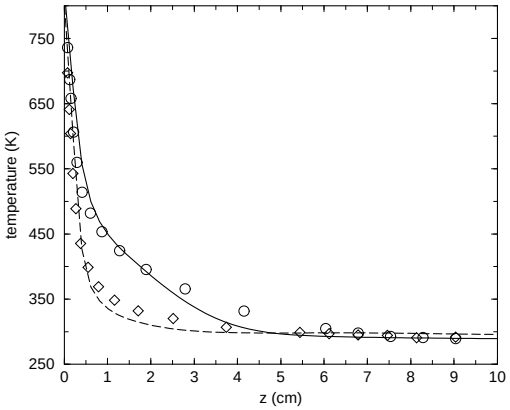

FIGURE 8. Comparison of calculated (lines) and measured (symbols) boundary layer temperature profiles at x=276 cm, y=252 cm (solid line and circles) and at x=276 cm, y=22 cm (dashed line and diamonds); mixed convection, ID648.

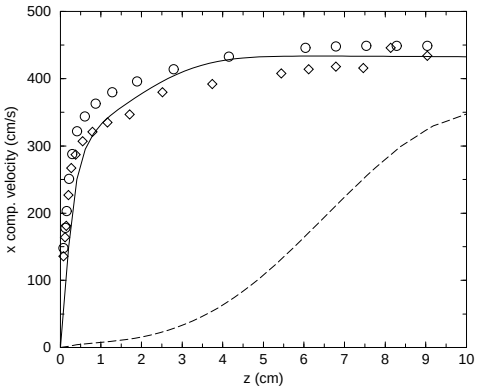

FIGURE 9. Comparison of calculated (lines) and measured (symbols) boundary layer x comp. velocity profiles at x=276 cm, y=252 cm (solid line and circles) and at x=276 cm, y=22 cm (dashed line and diamonds); mixed convection, ID648.

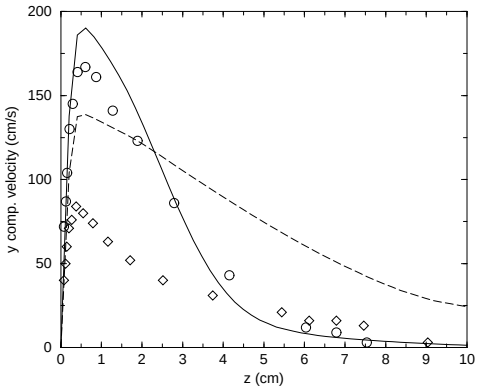

FIGURE 10. Comparison of calculated (lines) and measured (symbols) boundary layer y comp. velocity profiles at x=276 cm, y=252 cm (solid line and circles) and at x=276 cm, y=22 cm (dashed line and diamonds); mixed convection, ID648.

of temperature and x and y components of velocity near the vertical trailing edge of the plate (x=276 cm) and at two vertical locations (y=22 and 252 cm) are compared in figures 8, 9 and 10 respectively. The calculated results agree well with the data except for the velocity components at y=22 cm (near the bottom of the plate). Efforts are underway to compute this case at finer grid resolution.

The computed local heat-transfer coefficient for the mixed-convection case is compared with experimental data in figure 11 along a horizontal line on the plate at y=155 cm, and in figure 12 along a vertical line near the vertical trailing edge of the plate at $x \approx$ 270 cm. The results are in reasonable agreement with experimental data.

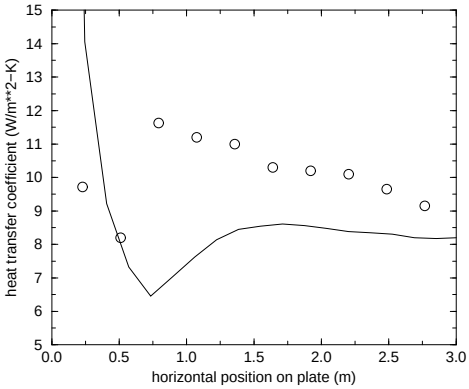

FIGURE 11. Comparison of calculated (line) and measured (symbols) local heat transfer coefficient on a horizontal line at y=1.55 m for the mixed convection case, ID648.

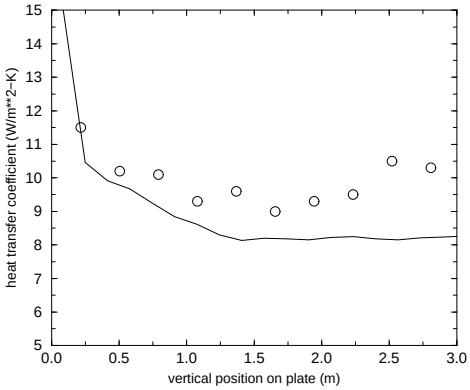

FIGURE 12. Comparison of calculated (line at x=269 cm) and measured (symbols at x=276 cm) local heat transfer coefficient on a vertical line at $x \approx$2.7m for the mixed convection case, ID648.

3. DNS of free convection

In the free-convection case of figure 1 ($\mathrm{Gr_H} = 1.4\mathrm{x}10^{12}$, $\mathrm{Re_L} = 0.0$), the experimental data of Siebers, Schwind & Moffat (1983) do not include boundary layer profiles below approximately 2 m above the bottom of the plate. In such cases, the upstream flow conditions near the bottom of the plate may be difficult to predict with RANS calculations such as the forced- and mixed-convection calculations presented in the last section. In particular, it may be difficult to predict where transition to turbulence occurs. The DNS results to be presented here for *free* convection help to answer such questions and provide higher-fidelity boundary-layer statistics against which to validate the RANS calculations. Free-convection RANS calculations are still in progress.

The spatial and temporal resolution requirements of DNS restrict the size of the domain to less than 20% of the vertical extent of Siebers' plate and less than 5% of its width. However, it is expected that the DNS data will also provide a benchmark for a future LES encompassing the full vertical extent of the plate. Figure 13 shows the DNS domain geometry and instantaneous temperature contours. The opaque boundary shown encompasses a 5cm tall, unheated, free-slip surface, above which is a 50 cm tall no-slip surface heated to 424 C. Above this no-slip surface is a 5 cm tall open surface. The two 5cm tall surfaces separate the heated region from the inflow and outflow boundary conditions to prevent these conditions from affecting the statistics collected in the heated region. In the wall-normal and spanwise horizontal directions, the flow domain is 3.75 cm and 10 cm wide, respectively. The above dimensions correspond to roughly 1730, 298, and 109 wall units in the streamwise (vertical), spanwise, and wall-normal directions, respectively.

All clear boundaries in figure 13 are open and allow inflow or outflow as the problem solution dictates. The numerical implementation of these boundary conditions will be described in section 3.2.

3.1. *Mathematical model*

The DNS was performed with the Fire Dynamics Simulator (FDS) published by the National Institute of Standards and Technology (see McGrattan, Rehm & Baum (1994), McGrattan, Baum & Rehm (1998)). FDS solves the low-Mach-number form of the compress-

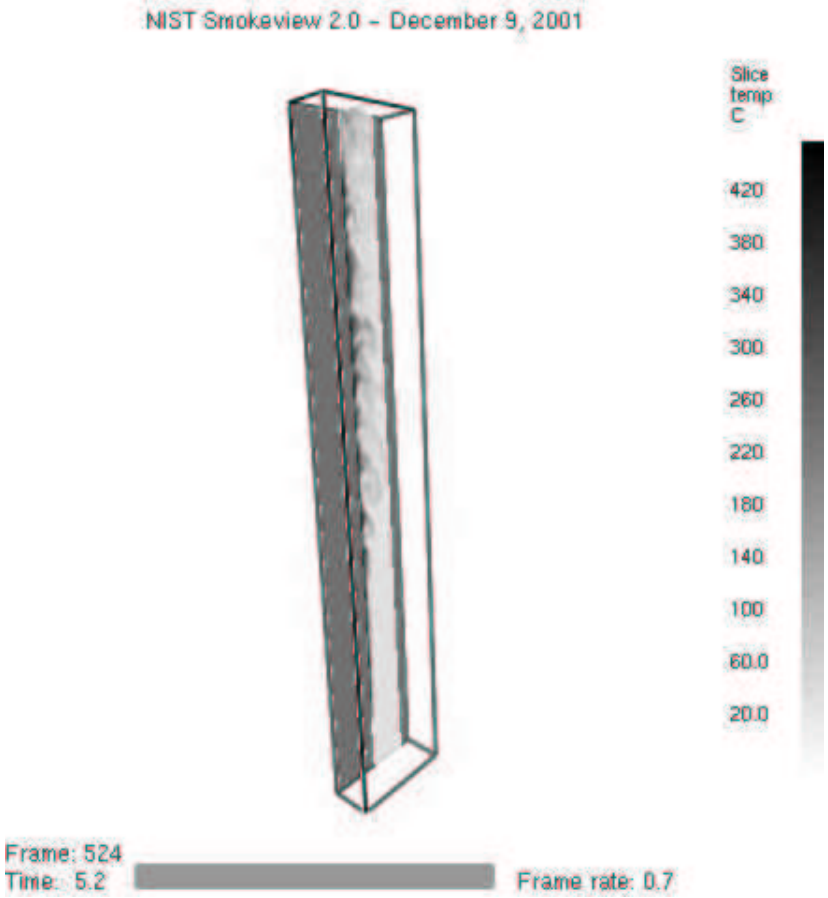

FIGURE 13. Geometry and temperature contours at the end of the DNS.

ible Navier-Stokes equations first proposed by Rehm & Baum. (1978). For a chemically -nert gas, these equations take the form

$$\frac{\partial \mathbf{u}}{\partial t} = \mathbf{u} \times \omega - \nabla \mathcal{H} + \frac{1}{\rho}(\rho - \rho_\infty)\mathbf{g} + \nabla \cdot \tau, \tag{3.1}$$

$$\frac{\partial \rho}{\partial t} + \mathbf{u} \cdot \nabla \rho = -\rho \nabla \cdot \mathbf{u}, \tag{3.2}$$

where $\mathbf{u}$, ω, and ρ are the fluid velocity, vorticity and density, respectively; ρ_∞ is a reference density; τ is the viscous-stress tensor given by

$$\tau = \mu \left[\nabla \mathbf{u} + (\nabla \mathbf{u})^T + \frac{2}{3}(\nabla \cdot \mathbf{u})\mathbf{I} \right], \tag{3.3}$$

where $\mathbf{I}$ is the identity tensor, and finally

$$\nabla \mathcal{H} \approx \frac{1}{2}\nabla |\mathbf{u}|^2 + \frac{1}{\rho}\nabla \tilde{p} \tag{3.4}$$

is an approximation that neglects baroclinic torques resulting from the non-alignment of the density and pressure gradients. In the last equation, $\tilde{p}$ is the pressure perturbation

in the following decomposition:

$$p = p_0 - \rho_\infty g z + \tilde{p}, \tag{3.5}$$

where p_0 is a background pressure,which remains constant in the present application and is given by the ideal gas law:

$$p_0 = \rho R T, \tag{3.6}$$

where T is the gas temperature and R is the gas constant divided by the molecular weight.

FDS uses fast Fourier transforms to solve the elliptic partial differential equation for $\mathcal{H}$ that results from taking the material derivative of p_0 and combining it with mass- and energy-conservation statements:

$$\nabla^2 \mathcal{H} = -\frac{\partial \nabla \cdot \mathbf{u}}{\partial t} - \nabla \cdot \mathbf{F}, \tag{3.7}$$

$$\mathbf{F} \equiv -\mathbf{u} \times \omega - \frac{1}{\rho}(\rho - \rho_\infty)\mathbf{g} + \nabla \cdot \tau, \tag{3.8}$$

$$\nabla \cdot \mathbf{u} = \frac{\gamma - 1}{\gamma p_0}(\nabla \cdot \nabla T - \nabla \cdot \mathbf{q}_r), \tag{3.9}$$

where γ is the ratio of specific heats, k is the thermal conductivity, and $\mathbf{q}_r$ is the radiative heat flux.

In all of the above equations, FDS accounts for variable properties. Since FDS is designed to model combustion, the dynamic viscosity is calculated for each species present according to

$$\mu_l = \frac{26.69 \times 10^{-7} (M_l T)^{1/2}}{\sigma_l^2 \Omega_\nu}, \tag{3.10}$$

where M_l and σ_l are the molecular weight and the Lennard-Jones hard-sphere diameter of the l^{th} species, and where Ω_ν is an empirical collision integral. Likewise, the thermal conductivity of the l^{th} species is

$$k_l = \frac{\mu_l c_{p,l}}{Pr}, \tag{3.11}$$

where the Prandtl number, Pr, is 0.7 and $c_{p,l}$ is the constant-pressure specific heat of species l.

3.2. *Numerical method*

The above equations are advanced in time using a second-order Runge-Kutta, predictor-corrector algorithm. Spatial derivatives are estimated with second-order-accurate finite differences on a rectangular grid, with scalar quantities assigned to the center of grid cells and vector quantities assigned to cell faces. Convective terms are upwind-biased, based on a CFL condition, in the predictor step and downwind-biased in the corrector step. Where the CFL number is near its upper limit, differencing is nearly fully-upwind. Where the CFL number is small, differencing is nearly centered. Diffusive terms are central-differenced. In the current problem, these differencing schemes are employed on a grid with $192 \times 96 \times 64$ points in the streamwise, spanwise and wall-normal directions resulting in spacings of 3.1, 9.0 and 1.7 wall units in these directions, respectively.

The initial condition is still air at standard temperature and pressure, to which FDS adds random vorticity perturbations resulting in velocites on the order of 1mm/s. These perturbations disrupt the flow symmetry that would othewise result from the specifi-

cat1on of symmetric boundary and initial conditions. As will be seen below, this has the effect of tripping the flow, causing unstable waves that decay into turbulence.

A homogeneous Neumann condition is applied to $\mathcal{H}$ at the no-slip boundary:

$$\frac{\partial \mathcal{H}}{\partial n} = 0, \tag{3.12}$$

where n is the direction normal to the boundary. At open boundaries, the boundary condition on $\mathcal{H}$ varies depending on the flow orientation:

$$\mathcal{H} = |\mathbf{u}|^2/2, \quad \text{outgoing} \tag{3.13}$$

$$\mathcal{H} = 0, \qquad \text{incoming.} \tag{3.14}$$

Other implementation details are described by McGrattan et al. (2001).

3.3. *DNS results*

Figure 13 shows temperature contours at the final time step after 5.2 s of physical time. Smooth, laminar contours can be discerned near the bottom of the domain with a rapid transition to turbulence between 10 and 20 cm from the bottom of the heated portion. This flow pattern is established after approximately 1.5 s. It is preceded by a very orderly temporal transition, illustrated in figure 14 which shows an instantaneous isothermal surface at 200 C in a run with a slightly higher wall temperature of 462 C and a resolution of only 64 points in the wall-normal direction. Apparent in the surface at 1.2s into the simulation is a dominant mode of oscillation extending over the vertical extent of the plate with little spanwise temperature variation except near the side boundaries where cold air is entrained. This orderly instability rapidly decays into a fully three-dimensional disturbance, yielding the disorderly surface shown in figure 15 after 1.6 s. Time traces (not shown) indicate that the above unstable mode results in a persistent, periodic oscillation in the temperatures and velocities 10 cm above the bottom of the plate. This periodic variation remains at this location throughout the simulation, while just above this location, the entire flow is turbulent after 1.5 s.

Figures 16–17 show time-averaged temperature and velocity profiles at a location 40 cm above the bottom of the heated portion of the plate. Although both plots agree qualitatively with typical free-convection profiles, the RANS calculations to which these will be compared are still under way and no data were were taken this low on the plate in the experiment. Calculating a heat-transfer coefficient from the temperature profile, and evaluating all properties at freestream conditions, the ratio $Nu_x/Gr_x^{1/3}$ is 0.173, where Nu_x is the Nusselt number based on height above the bottom edge of the plate and Gr_x is the Grashof number based on the same height. This value is is 80% higher than the value measured by Siebers, Schwind & Moffat (1983) in fully-turbulent flow. However, $Nu_x = 270$ and $Gr_x = 3.8 \times 10^9$ at this location in the DNS, which falls in the middle of the turbulent transition range in the experimental data.

4. Temporal filtering

The preceding sections have addressed convection heat transfer with the broadest range of filter widths from direct numerical simulation to traditional Reynolds averaging. Approaches that implicitly or explicitly involve filter widths between these limits, including large-eddy simulation, very-large-eddy simulation, detached-eddy simulation, and unsteady RANS (cf. Speziale (2000), Spalart (2000)). All but the last are filtered

FIGURE 14. Isothermal 200 C surface 1.2 s after the initial time.

FIGURE 15. Isothermal 200 C surface 1.6 s after the initial time.

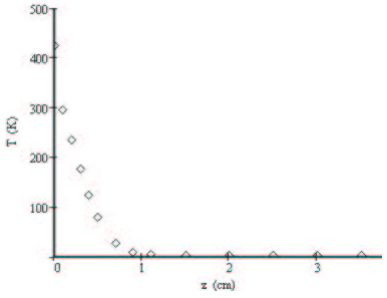

FIGURE 16. Temperature profile 40 cm above the bottom of the heated portion of the plate.

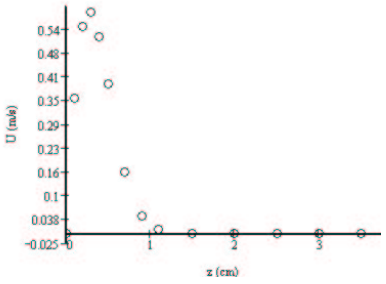

FIGURE 17. Vertical velocity profile 40 cm above the bottom of the heated portion of the plate.

in space: unsteady RANS is filtered in time. These techniques bridge the gap between fidelity and engineering practicality. The choice of method depends on application needs for these conflicting requirements.

Fire environments are strongly influenced by two modes of heat transfer, radiation and

convection, with radiation being dominant in most cases. In general, material response is dominated by conduction, and there is usually a significant separation between turbulent and material-response time scales. Thus, a substantial filter width can be employed for the reacting fluid mechanics without significant fidelity loss in material response. For this reason, it is desirable to use steady RANS approaches for maximum practicality.

On the other hand, to capture radiative emission, it is desirable to obtain as much spectral (temporal/spatial) resolution as possible from the Navier-Stokes solution because radiative emission is a highly-nonlinear process and is dominated by small-scale flame structures. Generally, the time-averaged output of a highly-nonlinear process is not strictly a function of time-averaged inputs. Specifically, the time-average flux is all that is required for material response, but the fidelity of subgrid radiative-emission models is limited by time-averaged scalar inputs. Further, fires are reacting plumes, and as such, there is strong coupling between the density and velocity fields. The coupling results in strong vorticity production, and turbulent dynamics produce large, coherent structures with a full turbulent cascade. For these reasons, it is desirable to resolve at least the large-scale, low frequency, structures within the flow.

Thus fire application requirements suggest a hybrid RANS/LES approach, retaining RANS in the near wall region of objects and LES in the bulk reacting flow. Most hybrid approaches, such as detached-eddy simulation, have employed spatial filtering of the Navier-Stokes equations, even though the RANS equations are temporally filtered. For this study, it was desired to explore temporal filtering as a means of separating the high-frequency wall boundary-layer region from the low-frequency puffing motion characteristic of fires.

Pruett (2000) explores temporal filtering for the Navier-Stokes equations and discusses its strengths and weaknesses. A strength is that temporal filters are bounded and thus the commutivity error usually associated with spatial filtering is generally avoided. Weaknesses include phase- and Doppler-shifting of the filtered signal. The phase-shifting occurs because temporal filters are by necessity causal, and hence one-sided. Doppler shifting occurs because the mean convective velocity increases the temporal frequency required to capture the signal of a given eddy size. Pruett (2000) concludes that the latter is the most serious drawback for use in applications for which it is desired to resolve eddies of a given size, i.e., traditional LES.

However, in the current application, temporal separation into structures of resolvable and unresolvable frequencies is perhaps a stronger motivation than separation of structures by size classification. Further, Courant-number limitations on numerical methods limit the time step, thus ensuring that convectively-induced Doppler shifting is minimized if the temporal filter width is some small multiple of the time step. Given the desire in current applications to employ RANS in the near-wall regions, a further advantage of temporal filtering is the consistency of the filtering operation, not requiring a shift from temporal- to spatial-filtering arguments inherent in hybrid RANS/LES approaches.

The current study represents an initial exploration of the practicality of temporal filtering within the time frame of the CTR summer program. In the next section, a simple eddy-viscosity model will be described, followed by a brief description of a test problem, comparison of model and data, and discussion.

4.1. *Implementation*

There are many possible closure models for the temporally-filtered equations. For this preliminary investigation, we chose a simple eddy-viscosity closure that retains the k-epsilon modeling in our RANS code. The definition ofintegral time scale in the standard

RANS eddy-viscosity formulation is replaced by a fixed temporal filter width which is input by the user.

$$\mu_t = \rho C_\mu k T \tag{4.1}$$

where

$$T = \min(t_f, k/\epsilon) \tag{4.2}$$

Selecting a fixed temporal time scale is analogous to selecting a fixed filter width in LES. If the selected filter width is larger than the integral scale, the min function selects the integral time scale. For this study the time step is fixed to one half the filter width.

The model has been implemented in FUEGO's predecessor, VULCAN (which is based on the KAMELEON family (cf, Holen, et al, (1990)), a staggered, block-structured grid code with second-order upwind differencing for the convective terms and a first order implicit (SIMPLE based) differencing for the transient term. In addition to the temporal filter, the k-epsilon implementation has a density based generation term (V. Nicolette, private communication). The model suite includes combustion, soot and radiation models.

4.2. *Test problem descriptions*

To test whether the current formulation will separate time scales, two problems with disparate time scales were simulated, the free convection data described earlier and recently published methane fire data Tieszen, et al, (2002). The methane data consists of a one meter high vertical plane of 2-D PIV data through the centerline of a one-meter-diameter methane fire (See citation for details). The experimental puffing frequency of the fire is 1.65 Hz.

4.3. *Model/data comparison*

Figures 18–25 show the results of the simulations, and comparisons with the methane data. The filter width for the results shown is 1/30 of the puffing period. Figure 18 shows the temperature profile at an instance in time. Figure 19 shows the simulated time history of the vertical velocity on the centerline, half a diameter above the burner. The puffing is somewhat irregular, as in the experiment, but consistent with the experimental value. Comparison of the vertical (axial) and horizontal (radial) time-averaged velocity fields is shown in figure 20 vs. figure 21, and figure 22 vs. figure 23, respectively. The width of the reacting mixing layers is somewhat underpredicted, resulting in the more-pronounced 'W' shape in the vertical velocity profile compared to the data. The transition from the 'W' shape to a Gaussian-like profile marks the end of the fuel vapor core in the fire.

Figures 24 and 25 compare the turbulent kinetic energy. The data assume that the out-of-plane fluctuations are comparable to the horizontal in-plane fluctuations. The simulation supports this assumption of the data analysis. Simulations with a filter width of 1/10 the puffing frequency (0.06 sec) still showed some dynamics, but were significantly more damped than those shown in the figures. Time-step and grid-refinement studies have yet to be conducted for a constant filter width.

Time did not permit simulations with the $v^2 f$ model for the free convection boundary layer. However, a preliminary simulation of the free convection problem using k-epsilon with no wall function with RANS mesh spacing of 7 cm parallel to the plate did not show any indication of puffing with a filter width of 0.05 sec as desired.

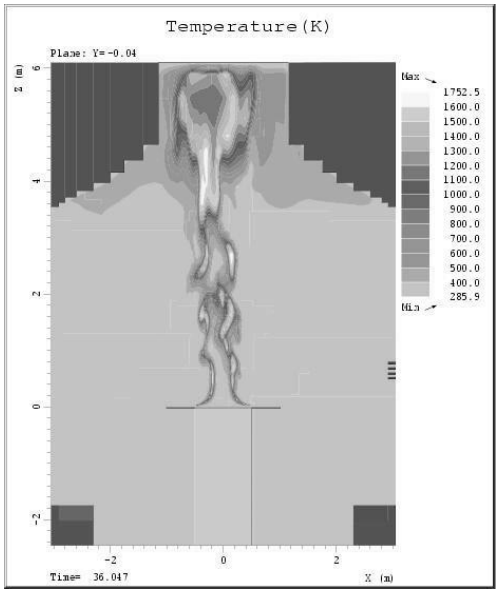

FIGURE 18. Instantaneous simulation temperature contours

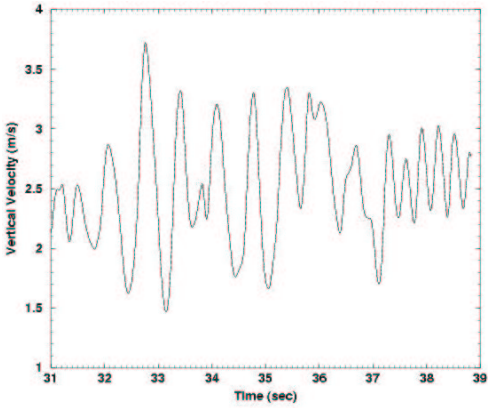

FIGURE 19. Vertical velocity vs time (Centerline at Z=0.5m)

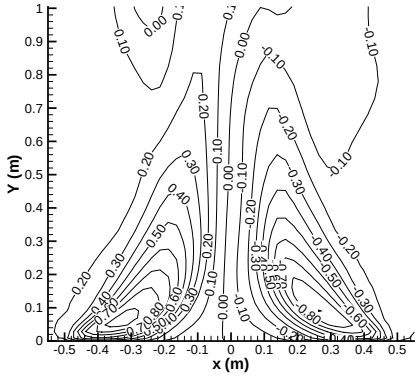

FIGURE 20. Radial Velocity (m/s) Simulation

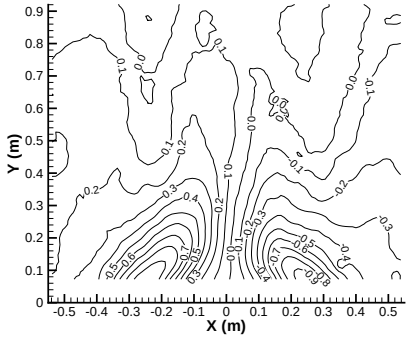

FIGURE 21. Radial Velocity (m/s) Experiment

4.4. *Discussion of temporal filtering*

Given the numerics and simple modeling closure, the preliminary comparisons are quite encouraging. Overall, the mixing is somewhat underpredicted. The underprediction may be due to an excess of numerical or model viscosity, or to physical reasons. Unlike momentum-driven flows, buoyant flows have strong coupling between the density and momentum fields. It can be argued that baroclinic vorticity production occurs at all scales in the cascade (Tieszen (2001)). Growth dynamics in the methane-fire mixing layer suggest that, via pairing, this small-scale production can result in large-scale dynamics. Eddy-viscosity models, which are designed for energy dissipation, do not capture the

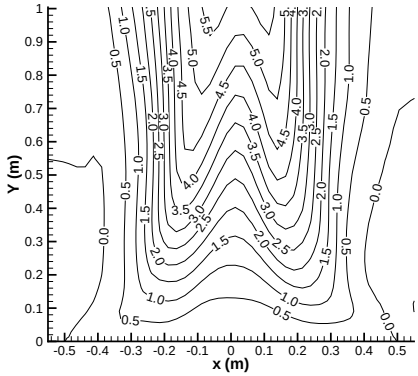

FIGURE 22. Axial Velocity (m/s) Simulation

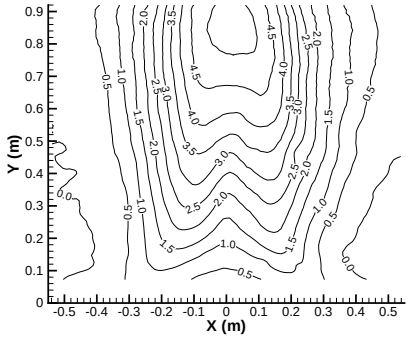

FIGURE 23. Axial Velocity (m/s) Experiment

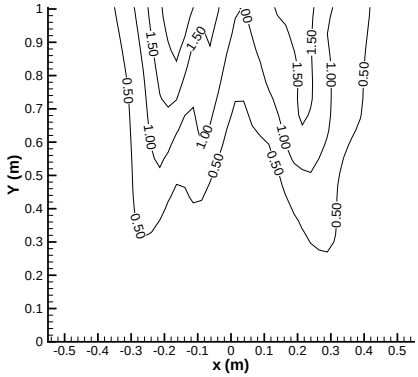

FIGURE 24. Turbulent Kinetic Energy (m^2/s^2) Simulation

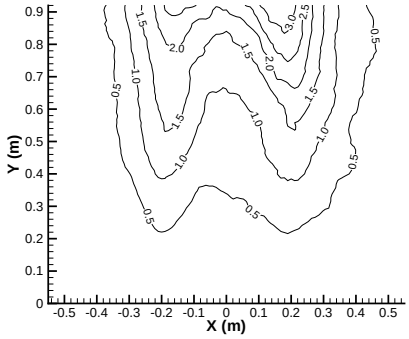

FIGURE 25. Turbulent Kinetic Energy (m^2/s^2) Experiment

vorticity production at small scales andits later appearance as vorticity at grid-resolved scales due to pairing mechanisms along the mixing layer.

5. Conclusions

Simulations of the three-dimensional turbulent flow and heat transfer adjacent to a large (3 meter) high-temperature (up to 860 K) vertical flat plate and in a large-scale methane flame have been made and compared with experimental data. Reynolds-averaged Navier-Stokes (RANS) results using the $v^2 - f$ model wall treatment of forced- and-fixed convection flow and heat transfer on a vertical flat plate with a horizontal forced flow are in qualitative agreement with experimental data, with quantitative comparisons awaiting finer-mesh results. Direct numerical simulation (DNS) results indicate that transition occurs within 10-20 cm above the bottom of the heated plate. The transition proceeds as an initially-orderly wave that convects along the entire vertical extent of the plate

before transition to turbulence. These insights have helped to inform the ongoing RANS development effort by providing a detailed picture of the upstream flow conditions where measurements were unavailable. Preliminary detached-eddy simulation (DES) comparisons for the methane fire are quite encouraging, although overall the mixing is somewhat underpredicted. For free convection on the heated plate, the preliminary DES results were steady as desired.

REFERENCES

Siebers, D. L., Schwind, R. G., & Moffat, R. J. 1983 Experimental Mixed Convection Heat Transfer From a Large, Vertical Surface in a Horizontal Flow. *SANDIA REPORT* SAND83-8225.

Moen, C. D., Evans, G. H., Domino, S. P. & Burns, S. P. 2002 A Multi-Mechanics Approach to Computational Heat Transfer. *proceedings IMECE2002-33098* to be presented at 2002 ASME Int. Mech. Eng. Congress and Exhibition, November 17-22, New Orleans.

Magnussen, B. F. 1989 Modeling of NOx and Soot Formation by the Eddy Dissipation Concept. *International Flame Research Foundation* 1st Topical Orientation Meeting, October, Amsterdam.

Launder, B. E. & Spalding, D. B. 1974 The Numerical Computation of Turbulent Flows. *Computer Meth. Appl. Mech. Eng.* **3**, 269-289.

Durbin, P. A. 1991 Near-Wall Turbulence Closure without Damping Functions. *Theoretical and Computational Fluid Dynamics.* **3**, 1-13.

Burns, S. P. 1997 Application of Spatial and Angular Domain Based Parallelism to a Discrete Ordinates Formulation with Unstructured Spatial Discretization. *2nd International Symposium on Radiation Transfer* ed. P. Mengüç, Int. Center for Heat and Mass Transfer, Kusadasi, Turkey.

Edwards, H. C. & Stewart, J. R. 2001 SIERRA: A Software Environment for Developing Complex Multi-physics Applications. *1st MIT Conf. on Computational Fluid and Solid Mechanics* ed. K. J. Bathe, Elsevier Scientific.

McGrattan, K., Rehm, R. G., & Baum, H. R. 1994 Fire-driven flows in enclosures. *J. Comp. Phys.* 110:285-291.

McGrattan, K., Baum, H. R. & Rehm, R. G. 1998 Large eddy simulation of smoke movement, *Fire Safety Journal* 30:161-178.

Rehm, R. G. & Baum, H. R. 1978 The equations of motion for thermally driven, buoyant flows, *Journal of Research of the NBS* 83:297-308.

McGrattan, K. B., Baum, H. R., Rehm, R. G., Hamins, A., Forney, G. P., & Floyd, J. E. 2001 Fire Dynamics Simulator (Version 2), Technical Reference Guide, Natl. Inst. Standards & Technology, *NISTIR 6783.*

Gran, I. R. & Magnussen, B. F. 1996 A numerical study of a bluff-body stabilized diffusion flame. Part 2. Influence of combustion modeling and finite-rate chemistry. *Combust. Sci. and Tech.* **119**, 191-217.

Holen, J., Brostrom, M., & Magnussen, B. F. 1990 Finite difference calculation of pool fires. *23rd Sympo.(International) on Combustion*, The Combustion Institute, pp. 1677–1683.

Pruett, C. D. 2000 Eulerian time-domain filgering for spatial large-eddy simulation. *AIAA J.* **38**, 1634–1642.

Spalart, P. R. 2000 Strategies for turbulence modelling and simulations. *Int. J. Heat and Fluid Flow.* **21**, 252–263.

Speziale, C. G. 1998 Turbulence modeling for time-dependent RANS and VLES: a review. *AIAA J.* **36**, 173–184.

Tieszen, S. R. 2001 On the fluid mechanics of fires. *Annu. Rev. Fluid Mech.* **133**, 62–92.

Tieszen, S. R., O'Hern T. J., Schefer, R.W., Weckman, E. J.,& Blanchat, T. K. 2002 Experimental study of the flow field in and around a one meter diameter methane fire. *Combust. Flame* **129**, 378–391.